

10



Spatiotemporal Characterization of Wheat Development Using UAV LiDAR Structure–Intensity Fusion with Multispectral and Thermal Data

Jordan Steven Bates^{1 2}, Carsten Montzka², Rajina Bajracharya ³, Harry Vereecken ², François Jonard ¹

¹ Earth Observation and Ecosystem Modeling (EOSystM) Laboratory, SPHERES Research Unit, University of Liege, Liege, Belgium

² Institute of Bio- and Geosciences: Agrosphere (IBG-3), Forschungszentrum Jülich GmbH, 52428 Jülich, Germany

³ Institute of Rural Studies, Thünen Institute, 38116 Braunschweig, Germany

Correspondence to: Jordan Steven Bates (j.bates@uliege.be)

Abstract: This study presents the first integration of UAV LiDAR structure (canopy height (CH), multi-layer gap fraction (GF)) and intensity features with multispectral (MS) and thermal infrared (TIR) data for aboveground biomass (AGB) estimation in winter wheat. A shallow artificial neural network (ANN), trained on a limited but high-quality destructive dataset, enabled direct integration of multi-sensor features without complex parameterization, supporting systematic evaluation of individual and combined sensor performance. Among single-sensor inputs, LiDAR features were most effective. LiDAR alone, combining all of its features such as CH, multi-layer GF, and INT, achieved a testing RMSE of 1.73 t/ha (18.27% error) and R² = 0.87, surpassing the common reliance on CH or MS features in UAV-based AGB studies. Multi-layer GF also improved accuracy compared to conventional ground-return GF and was successfully used as a direct ANN input. Fusion with other sensors further enhanced performance, with the best model (LiDAR INT + MS + TIR) reaching a testing RMSE of 1.47 t/ha (16.3% error) and R² = 0.91. Notably, this outperformed fusion models that included LiDAR CH or GF, indicating that INT is a particularly information-rich predictor likely encoding both structural and physiological canopy properties. Furthermore, sensor contributions varied seasonally, with CH and GF most informative during early growth and canopy closure, while MS and TIR became dominant during senescence and stress, with rankings providing practical guidance for sensor selection based on monitoring periods or economic constraints. Results from nitrogen treatments indicated that UAV data captured management effects more effectively than destructive sampling, highlighting the value of spatially comprehensive observations, an advantage that can be further enhanced through the fusion of emerging UAV sensor products. Overall, the findings position LiDAR's dual structural and spectral information, particularly INT, as a promising breakthrough for improving UAV-based AGB monitoring, with strong potential to advance multi-sensor fusion approaches as algorithms and crop applications broaden.

Keywords: Drone; multi-sensor, machine learning, AI, biomass





1 Introduction

Above-ground biomass (AGB) is a key indicator of crop growth and photosynthetic productivity, essential for yield prediction and data-driven management in precision agriculture (Bazrafkan et al., 2023; Lu et al., 2019). Conventional methods like manual sampling are labor-intensive and lack field-scale coverage (Pan et al., 2022). While satellite remote sensing offers broader spatial data, it is limited by cloud cover, revisit times, and insufficient resolution for within-field variability (Wang et al., 2021). Manned aircraft are costly for frequent monitoring, and ground-based systems, though accurate, are constrained by limited mobility, operational risks, and potential soil compaction (Wang et al., 2021; Johansen et al., 2020). In contrast, unmanned aircraft vehicles (UAV) provide flexible, high-resolution, and on-demand data acquisition, operating below cloud cover with minimal atmospheric interference, making them ideally suited for AGB assessment in precision agriculture.

45

50

55

UAV platforms support an expanding array of sensor technologies, with the most common including RGB, multispectral (MS), thermal infrared (TIR), and light detection and ranging (LiDAR) systems (Bazrafkan et al., 2023). Among these, MS sensors are most widely used for biomass estimation, capturing reflectance in visible (VIS) and near-infrared (NIR) spectral bands to compute vegetation indices (VIs) that are strongly correlated with photosynthetic activity and crop vigor (Biswal et al., 2024). MS data have been applied to estimate chlorophyll content, nitrogen concentration, leaf area index (LAI), fractional vegetation cover, and yield potential (Caturegli et al., 2016; Yang et al., 2018). TIR sensors, by contrast, measure land surface temperature (LST), which is closely linked to plant water stress and stomatal conductance (Ludovisi et al., 2017; Smigaj et al., 2024). When combined with meteorological data, TIR observations support the estimation of key physiological indicators such as the crop water stress index (CWSI) and evapotranspiration (ET) (Berni et al., 2009). Although TIR data have also been used for biomass estimation, studies generally report lower accuracy compared to MS sensors (Li et al., 2024; Maimaitijiang et al., 2017).

60

As opposed to the passive optical sensors, LiDAR provides three-dimensional data on crop structure and is valuable due to its ability to penetrate vegetation and collect data unaffected by shadowing (Neuville et al., 2021; Wang et al., 2017). Structural properties such as crop height (CH) have shown significant promise in many cases as a strong indicator of AGB (Pan et al., 2022; Li et al., 2024; Bendig et al., 2014; Madec et al., 2017) particularly as compared to MS data, which often experiences saturation issues (Vahidi et al., 2023). With LiDAR systems being recently miniaturized enough for UAV use, they have become a more preferred method of estimating CH, offering greater precision compared to passive sensing techniques like RGB sensors and structure-from-motion (SfM) photogrammetry (Liao et al., 2021; Wallace et al., 2016). While SfM remains the more affordable alternative, LiDAR provides additional valuable outputs, including gap fraction (GF) and signal return intensities. LiDAR's ability to penetrate canopy gaps allows for the assessment of canopy density linked to LAI (Bates et al., 2021) and AGB (Montzka et al., 2023). Furthermore, the intensity of LiDAR signals, many of which operate in the NIR range (Kim et al., 2009), are sensitive to the plant biochemistry and in particular uses have found to be correlated with green area



75

95

100



index (GAI) (Liu et al., 2017), LAI (Luo et al., 2018), and nitrogen content (Hütt et al., 2022) as well as used for vegetation classification (Mesas-Carrascosa et al., 2012; Scaioni et al., 2018; Wu et al., 2021). It is therefore not surprising that UAV-based LiDAR intensity has also demonstrated predictive power in estimating AGB (Montzka et al., 2023; Hütt et al., 2022; Bates et al., 2022).

Integrating multiple sensor types can overcome limitations associated with individual data sources. For example, LiDAR can mitigate signal saturation issues commonly encountered in MS data, thereby improving the robustness of biomass estimation models (Tilly et al., 2015). Similarly, although TIR sensors alone often perform poorly for AGB estimation, they have been shown to enhance MS-based models when used in combination (Li et al., 2024). These benefits underscore the value of sensor fusion, particularly when paired with machine learning (ML) techniques capable of handling diverse input data.

Data fusion methods increasingly rely on ML to integrate multi-sensor information for vegetation monitoring (Li et al., 2024; Wang et al., 2024; Melitha et al., 2025). Artificial neural networks (ANNs) are particularly suited for this task, as they can capture nonlinear interactions among diverse sensor features and have often outperformed traditional approaches (Vahidi et al., 2023). Additionally, ANNs have become one of the predominate methods within crop yield prediction (Van Klompenburg et al., 2020). While multiple linear regression (MLR) remains common for UAV-based AGB estimation (Wang et al., 2021), ANNs provide greater flexibility by iteratively optimizing weights through backpropagation, which improves robustness against collinearity and noise (Dawidowicz et al., 2024; Huang et al., 2022). Compared with support vector machines (SVMs), which require kernel selection and can be prone to overfitting with small datasets, ANNs offer a straightforward framework for continuous regression on tabular sensor features. Prior studies have demonstrated that ANNs match or exceed the performance of MLR and SVM for crop trait and yield estimation (Kidson et al., 2025; Abu Jabed et al., 2024; Lionel et al., 2025), supporting their use here for fusing and evaluating UAV-based multi-sensor features.

This study aims to improve UAV-based AGB estimation by fully leveraging the structural and spectral capabilities of LiDAR in combination with MS and TIR sensors. While prior studies have explored individual LiDAR-derived metrics such as CH, GF, or signal intensity (INT), no research to date has evaluated the combined predictive power of all three LiDAR features, nor their integration with MS and TIR data, for season-long biomass monitoring. Moreover, the potential of multi-layer GF for capturing vertical canopy heterogeneity remains underexplored, despite growing evidence that LiDAR parameter choices affect estimation accuracy (Wang et al., 2021). To address these gaps, this study first optimizes and extends existing GF methods by incorporating multi-layer vertical segmentation to enhance structural resolution. It then systematically evaluates the performance of LiDAR-derived features, MS, and TIR, individually and in fusion, across key wheat growth stages. In doing so, this work develops a comprehensive understanding of how sensor performance varies temporally and identifies optimal combinations. The results aim to provide practical guidance for UAV sensor selection and integration, ultimately supporting scalable, season-long monitoring of crop development and nitrogen-related dynamics in precision agriculture.

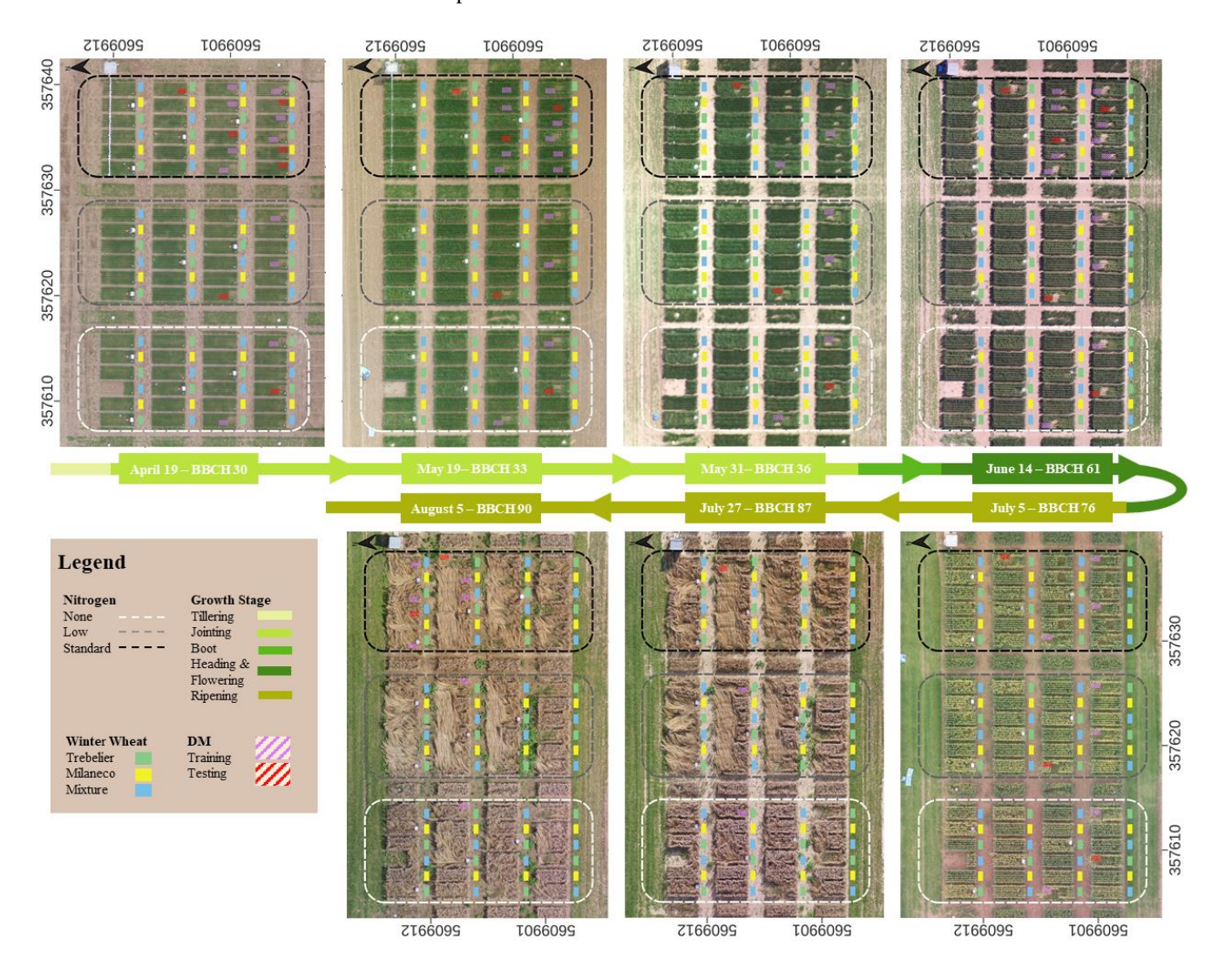




2 Experiment Site and Setup

The study was conducted at the PhenoRob Central Experiment site at Campus Klein Altendorf (CKA), Germany, characterized by a temperate oceanic climate (altitude: 176 m, average annual precipitation: 603 mm, and temperature: 9.4°C). The winter wheat field was selected for its homogeneous soil and nitrogen conditions, verified by prior (unpublished) soil conductivity mapping. For further information about the soil properties of the experiment area see the study of Seidel et al. (2024).

The experiment consisted of 12 main plots, each subdivided into six 1.5 × 3 m subplots (6 rows). These were organized into three nitrogen (N) treatment zones: 0%, 50%, and 100% (50 kg N/ha using a 30% N ammonium nitrate-urea solution), applied on March 24, April 20, and June 7. Two wheat genotypes, Trebelier (shallow rooting) and Milaneco (deep rooting), and a mixture of both were alternated across the subplots.





130

135

140



Figure 1: Study area and winter wheat experimental setup across all UAV data acquisition dates and destructive biomass sampling, covering the growth period from the beginning of jointing to the end of the ripening phase. The experimental field was divided into three zones based on different nitrogen fertilization levels. Within each zone, subplots were assigned to one of three genotype categories: Trebelier, Milaneco, or a mixture of both. Locations of destructive biomass measurements (DM) are marked and color-coded according to their use in either model training or testing.

AGB destructive samples were collected in sync with UAV flights from April 19 to August 5, 2021. Samples (75 cm of two rows) were taken from internal rows to reduce edge effects, dried at 60°C for ≥48 hours, and weighed in t/ha. Trebelier was sampled biweekly, while Milaneco was sampled monthly. Regional flooding in July reduced samples for late-season flights. Figure 1 shows the experimental layout and sampling overview.

3 UAV Data and Pre-processing

Two DJI Matrice 600 hexacopters were used to enable a multi-sensor workflow. One was equipped with a YellowScan Surveyor LiDAR system (Velodyne VLP-16 scanner and Applanix APX15 GNSS-Inertial unit), and the other carried a MicaSense RedEdge-M MS sensor and a FLIR Vue Pro R TIR sensor mounted on a DJI Ronin gimbal.

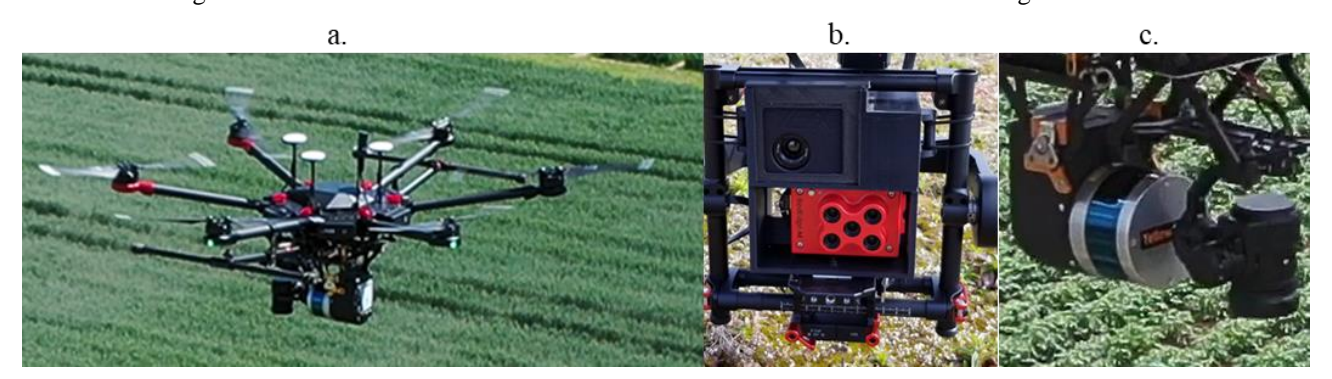


Figure 2: (a.) The DJI Matrice 600 equipped with the Yellowscan LiDAR Surveyor and the DJI Zenmuse X1 RGB camera, (b.) the FLIR Vue pro R TIR sensor on top and Micasense RedEdge-M MS sensor on bottom mounted to the DJI Ronin gimbal, and (c.) a closer look at the LiDAR and RGB setup. Note: RGB camera was only used for study area images seen in Figure 1.

The LiDAR system operates in the NIR spectrum (897–907 nm), emitting 300,000 pulses per second with ~4 cm precision. Flights were conducted at 8 m/s and 50 m altitude using a double-grid pattern, ±25° scan angles, and 50% side overlap. GNSS corrections from a Septentrio Altus NR3 base station supported post-processing in Applanix POSPac and YellowScan CloudStation to generate accurate point clouds. The MS sensor collected data in the red (663–673 nm), red-edge (712–722 nm), and NIR (820–860 nm) bands. The TIR sensor (7.5–13.5 μm) was calibrated using internal radiometric parameters (e.g., emissivity, air temperature, humidity) and a metallic blackbody ground target. An external heated shutter (TEAX ThermalCapture) was added to improve microbolometer drift correction, potentially enhancing accuracy by up to 70% (Virtue et al., 2021). The MS and TIR flights were conducted at 100 m altitude and 6 m/s with 90% overlap in a single-grid pattern. MS calibration was performed using a reflectance panel. All imagery was processed in Pix4D to generate georeferenced orthomosaics, with further raster and LiDAR point cloud analysis conducted in RStudio using the lidR and raster packages.



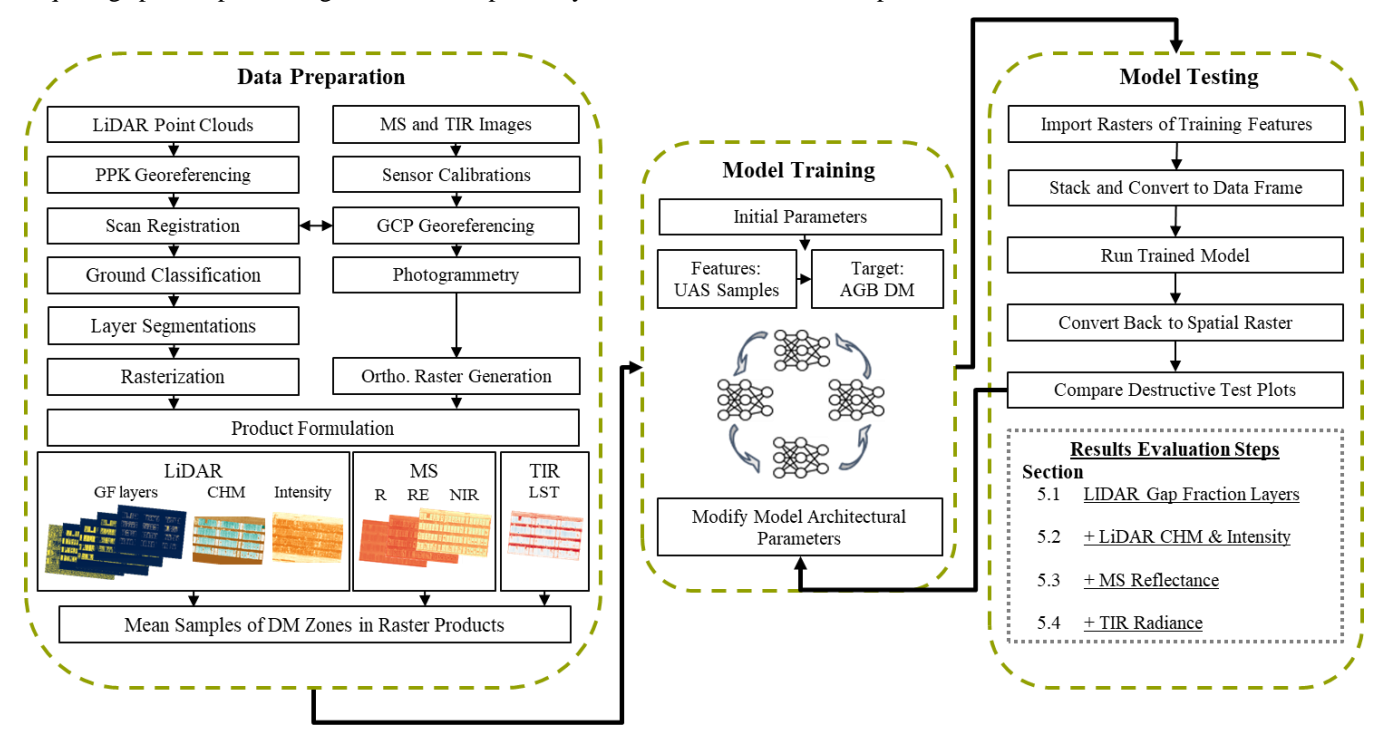


4 Methods

150

155

The workflow as seen in Figure 3 was used to estimate AGB using ANN models. Each sensor type produced unique data requiring specific processing to ensure compatibility and relevance for model input.



145 Figure 3: Workflow of the study from preparation of the data types to the model training with iterations in architecture based on input features, and data reformatting, model testing, and results per a tier step process in evaluation.

LiDAR data provided high-density 3D point clouds used to derive structural metrics (CH, GF) and signal intensity (INT). MS and TIR sensors delivered spectral data in red (R), red-edge (RE), near-infrared (NIR), and thermal bands. The distinctions between these sensor products are visually summarized, including spectral properties of MS reflectance and TIR radiance, in Figure 4. These outputs were georeferenced, resampled, and aligned to ensure consistent spatial resolution. Raster datasets were sampled using subplot shapefiles corresponding to destructive AGB sampling areas, enabling zonal statistics extraction for ANN training and validation. Ground points were identified using the Cloth Simulation Filter (CSF) (Zhang et al., 2016), which efficiently separates terrain and vegetation in LiDAR data. A grid resolution of 4 cm was used, consistent with sensor precision. These ground points served as the spatial reference for GF calculations and for normalizing signal intensity explained in more detail in Sections 4.2 – 4.3. To enable ANN-based modeling, all input metrics were standardized. Raster inputs were converted to data frames with geographic metadata stripped and values normalized to the 0–1 range. Once predictions were computed, spatial information was reattached to generate AGB estimation rasters at the pixel level. Input features and parameters (e.g., number of hidden nodes/layers, activation functions) were optimized through iterative evaluation, with training and testing performance assessed using RMSE and R² metrics. Each model was trained using zonal mean sensor values



170

175

180



per subplot and validated against dry matter (DM) AGB ground truth data. The best-performing ANN models for each sensor or fusion configuration were retained for generating full-field AGB maps.



Figure 4: Comparison of the sensory type metrics and differences with structural products including LiDAR gap fraction (GF) and LiDAR crop height model (CHM), and spectral products including the LiDAR signal intensity, multispectral reflectance, and thermal infrared radiance. Note: GF = gap fraction; $n_{DL} = point$ count for particular point density layer; n = point count of all layers within grid cell; CHM = crop height model; $DSM_d = digital$ surface model for respective day in the growing season; $DTM_0 = digital$ terrain model before vegetation growth.

A tiered approach was used to systematically evaluate the impact of different input features. First, optimal configurations for LiDAR GF were identified by testing multi-layer segmentation schemes (Section 5.1). Second, we incorporated LiDAR CH and INT individually and in combinations (Section 5.2). Third, MS spectral reflectance bands were added (Section 5.3), followed by the inclusion of TIR features (Section 5.4). All analyses used a consistent resolution and were aligned to the best-performing GF configuration. Further details on the sensor products used are provided in Sections 4.1-4.5.

4.1. LiDAR Crop Height

CH was derived by subtracting the digital terrain model (DTM) from the digital surface model (DSM), with the DTM generated from UAV LiDAR data collected under bare-soil conditions prior to planting. This approach minimizes interpolation errors and improves accuracy (Cao et al., 2019). Several CH-derived metrics (e.g., mean, maximum, standard deviation) were tested, but the maximum CH per pixel was selected because it consistently showed stronger correlations with AGB in vertically structured, dense crops such as wheat (Bazrafkan et al., 2023). By focusing on a single robust height metric, we reduced feature redundancy and model complexity, helping to limit overfitting in small-sample conditions (Ruwanpathirana et al., 2024). Correlations of alternative CH metrics with AGB are provided in Appendix Figure A1.

4.2. LiDAR Gap Fraction

Traditional GF metrics estimate canopy density by comparing ground returns to total LiDAR points, often within Beer–Lambert formulations for LAI estimation (Heiskanen et al., 2015; Richardson et al., 2009). However, this approach loses reliability in dense wheat canopies where laser penetration to the ground is limited (Sabol et al., 2014). To capture vertical



200



canopy structure more effectively, we derived normalized density layers (nDL) that describe the distribution of LiDAR returns across the canopy profile. A related approach, the 3D Point Index (3DPI), normalizes point density by total returns and links the layers to LAI or AGB through linear relationships requiring calibration with an extinction coefficient (Jimenez-Berni et al., 2018). In contrast, our method normalized density layers into GF layers and used them directly as ANN inputs, removing the need for additional parameterization. This allowed the ANN to learn the relative contributions of each canopy layer dynamically across biomass variability and phenological stages, rather than relying on fixed extinction assumptions.

To evaluate the sensitivity of GF metrics to vertical and horizontal discretization, we tested four vertical segmentation schemes, ground-only (GND), three 30 cm layers, five 20 cm layers, and ten 10 cm layers (e.g., Figure 5a) at horizontal resolutions of 10, 20, and 30 cm. This systematic testing provided insights into the scale at which canopy density information is most informative for AGB estimation in relation to the sensor characteristics, parameterization choices, and LiDAR point density in this study (Section 5.1).

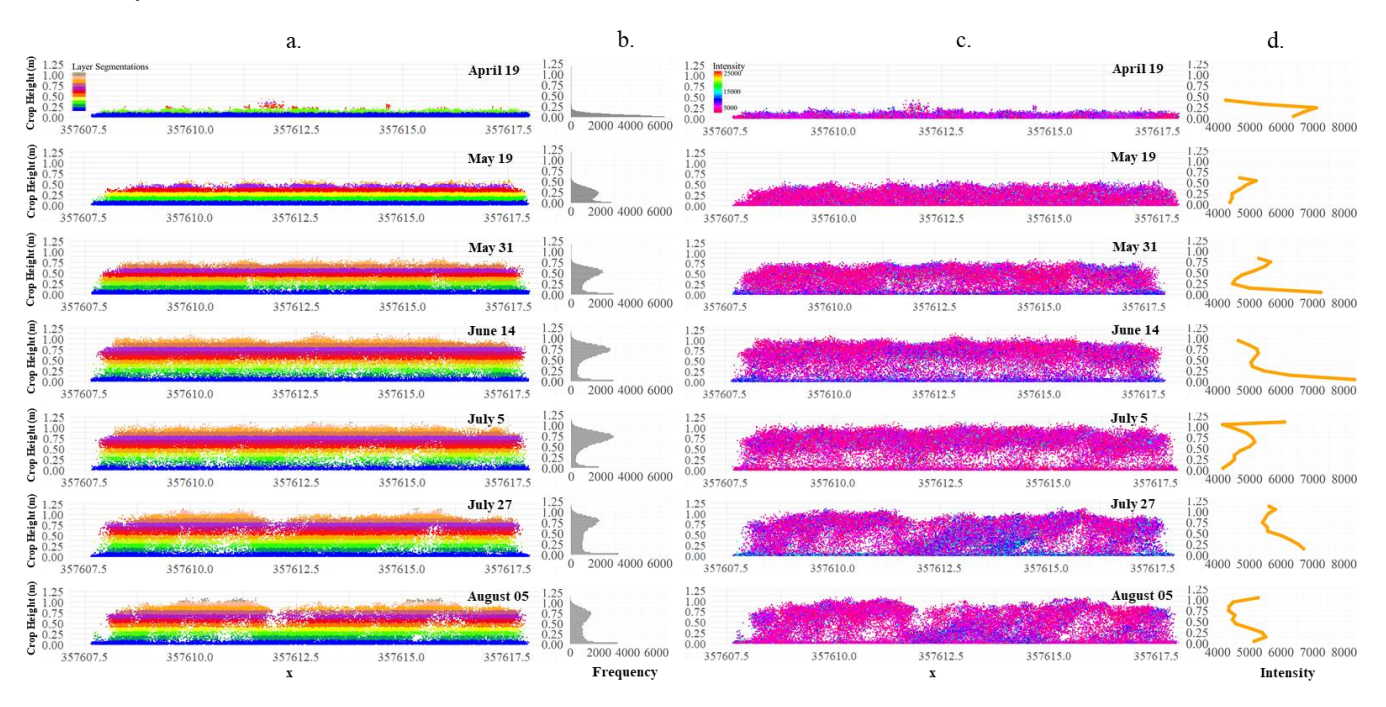


Figure 5: (a.) Cross section of subplot showing the LiDAR point allocation along the vertical extent of the canopy colored by 10cm layers. (b.) Histogram of point frequency throughout the vertical extent of the canopy. (c.) Cross section showing LiDAR signal intensity values throughout the canopy. (d.) Histogram of average intensity values throughout the vertical extent of the canopy.

4.3. LiDAR Intensity

LiDAR intensity reflects the strength of the return signal and is measured at 903 nm (NIR) making it sensitive to biochemical properties (Eitel et al., 2014). We used a maximum scan angle of 25° to minimize light dispersion, footprint variation, and further incident angle effects, leading to improved signal consistencies (Li et al., 2016).





205

210

220

235

The temporal use of LiDAR intensity data presents challenges, particularly due to environmental factors such as soil surface moisture, which can influence signal consistency. Without reflectance targets, ground intensity values provide a means for temporal calibration of vegetation intensity values. Luo et al. (2018) and Hütt et al. (2022) both discuss the noise introduced from ground intensity values when observing vegetation intensity leading to the need for correction. Airborne LiDAR studies have employed techniques such as the Light Penetration Index (LPI), which relates ground intensity to overall intensity distributions to improve LAI estimation (Solberg et al., 2006; Saskai et al., 2016; You et al., 2007). In this study, we adopt a comparable method where intensity values were normalized using ground returns across the field to reduce temporal variability caused by environmental effects such as moisture. This normalization enhances the comparability of intensity values across dates, improving their utility for AGB estimation.

215 4.4. MS Reflectance

MS data were collected in the red (R), red-edge (RE), and near-infrared (NIR) bands, which are highly sensitive to canopy vigor, chlorophyll status, and AGB and form the basis of many common vegetation indices (VIs) (Han et al., 2019). The RE band is particularly valuable as it is less prone to saturation at high AGB compared to the R band, making it a strong complement to NIR (Gitelson et al., 2003). In this study, the raw reflectance bands were used directly as ANN inputs rather than being combined into predefined VIs. This approach avoided redundancy among highly correlated indices and allowed the ANN to learn optimal nonlinear or weighted combinations of spectral features. Using raw bands also ensured that potentially unique information in each band was retained, which might otherwise be lost or averaged in conventional VIs.

4.5. TIR Radiance

TIR data were used to derive LST, which provides a direct measure of crop thermal status. However, LST is strongly influenced by background weather conditions, particularly air temperature, making it difficult to compare across dates or growth stages. To address this, LST was also converted to CWSI, which normalizes canopy temperature against reference "wet" and "dry" limits identified from seasonal temperature extremes and air temperature (Katimbo et al., 2022). In this way, CWSI provides a relative indicator of plant water stress that is less sensitive to temporal variability in atmospheric conditions. Both raw LST and normalized CWSI were included as predictors in the ANN models to assess whether absolute canopy temperature or a normalized stress index offered stronger explanatory power for AGB estimation. This dual use allowed evaluation of the trade-off between absolute thermal signals and temporally stable stress indicators within sensor fusion frameworks.

4.6. ANN Model

A multilayer perceptron ANN with backpropagation was implemented using the neuralnet package in RStudio. Model complexity (number of hidden layers and neurons) was optimized through iterative sensitivity testing, where one to two hidden layers with 2–14 neurons were evaluated. A linear (identity) activation function was applied, appropriate for continuous

https://doi.org/10.5194/egusphere-2025-5336 Preprint. Discussion started: 2 December 2025

© Author(s) 2025. CC BY 4.0 License.



240

245

250

255

EGUsphere Preprint repository

regression tasks. Training employed resilient backpropagation, the default optimizer in neuralnet, which performs full-batch weight updates each iteration. Accordingly, batch size is not applicable in this framework. Training was capped using stepmax $= 1 \times 10^6$ (maximum number of weight updates) and threshold = 0.01 (convergence criterion). These settings are functionally equivalent to defining a high maximum number of epochs with an early-stopping condition. All sensor features were normalized to a 0-1 range.

A total of 86 destructive AGB samples were available, with 70% used for training and 30% for testing. This sample size reflects the constraints of destructive biomass collection, which is highly labor-intensive and logistically limited when covering an entire growing season in parallel with other field experiments (Han et al., 2019; Wallace et al., 2017). The number and quality of destructive samples collected match or exceed what is typically reported in comparable UAV studies (Bendig et al., 2014; Morgan et al., 2025; Smith et al., 2024). The samples spanned seven campaigns with distinct growth stages, providing a wide range of canopy conditions and spectral–structural variability to provide generalizability between sensor features and biomass. Given the modest sample size, overfitting was a primary concern. To mitigate this risk, the ANN architecture was intentionally kept shallow, inputs were normalized, and model performance was always assessed by comparing RMSE and R² between training and testing subsets. A good fit is indicated by low errors in both sets with only a small generalization gap, while large discrepancies signal overfitting.

After validation, the trained ANN was applied to rasterized UAV data. All predictor rasters were co-registered, resampled, and stacked. The normalized raster stack was then passed through the trained network using the compute() function to generate spatially continuous AGB predictions. The resulting biomass maps were exported as GeoTIFFs with a UTM Zone 32N projection for visualization and further analysis.

5 Results

5.1. Gap Fraction Layer and Resolution Sensitivities

The GF approach was evaluated by adjusting two primary parameters: the depth of the density layers converted to gap fraction layers and the horizontal grid dimensions along the X and Y axes.



270



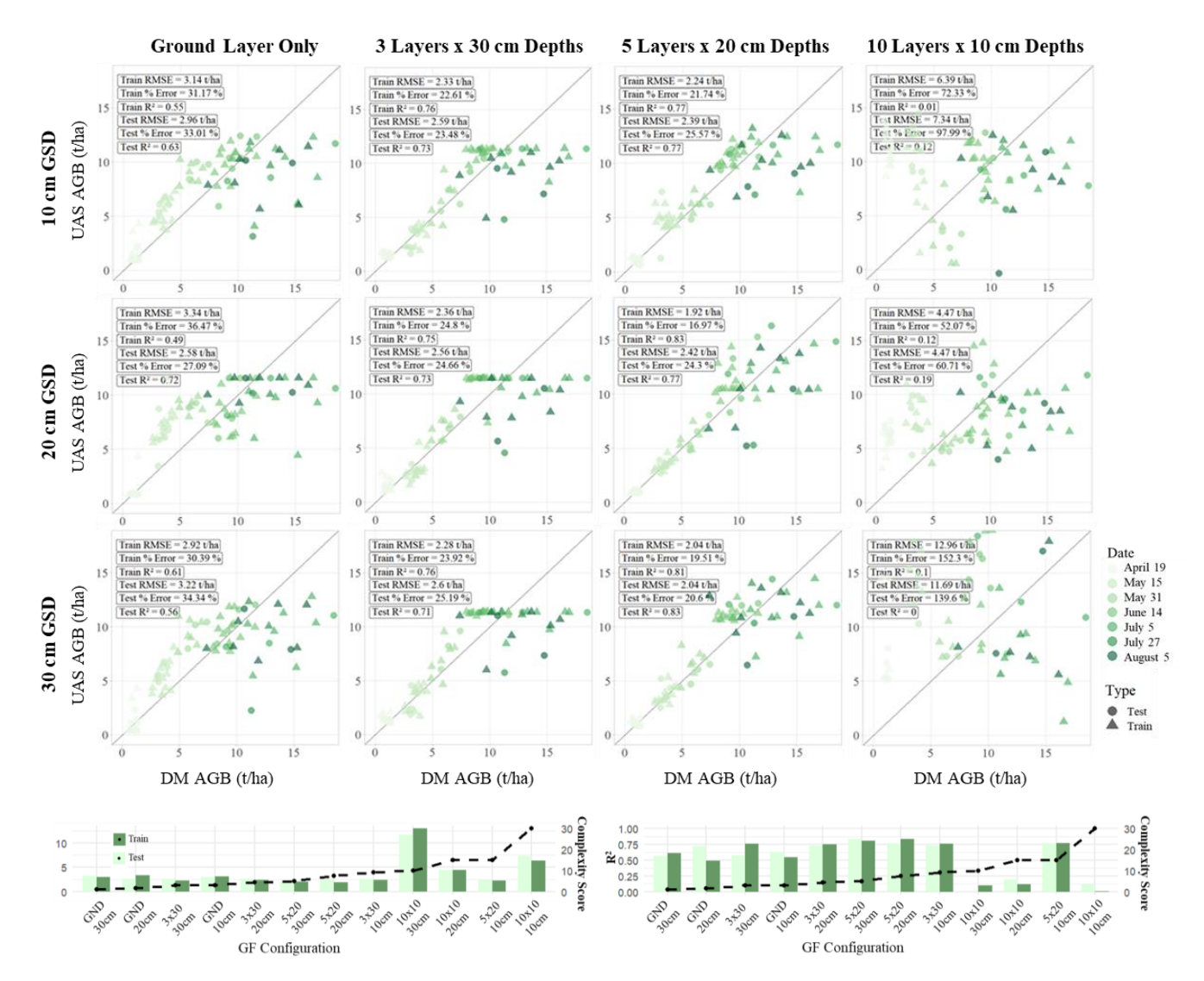


Figure 6: Top panel: Performance of ANN models trained using different LiDAR gap fraction (GF) configurations. Columns represent increasing vertical segmentation (from ground-only to 10×10 cm layers), and rows represent decreasing ground sampling distance (GSD). Models were evaluated using RMSE and R² on training and testing data. Bottom panel: Comparison of training and testing RMSE and R² values across GF configurations, including perceived model complexity. Complexity was calculated as the product of vertical layers and GSD resolution: Complexity = (Number of Layers) \times (30 / GSD in cm).

Overall, the configuration with five 20 cm vertical layers and a 30 cm GSD achieved the best performance (RMSE = 2.04 t/ha, $R^2 = 0.81 \text{ training}$; RMSE = 2.04 t/ha, $R^2 = 0.83 \text{ testing}$), demonstrating a clear advantage in capturing canopy structure. Simpler configurations using only GND returns or coarser vertical layers (3 x 30 cm) produced moderate results but failed to differentiate dense canopy structures during peak growth stages. Conversely, overly fine segmentations (10 x 10 cm)





significantly degraded performance, likely due to data sparsity and overfitting (e.g., RMSE = 7.34 t/ha, R² = 0.12 testing). These findings highlight the importance of balancing spatial granularity with model robustness when parameterizing LiDAR-derived GF.

5.2. Incorporation of LiDAR Height and Intensity with Gap Fraction

We next evaluated whether structural (crop height, CH) and spectral (LiDAR intensity, INT) features could compare or improve upon GF models.

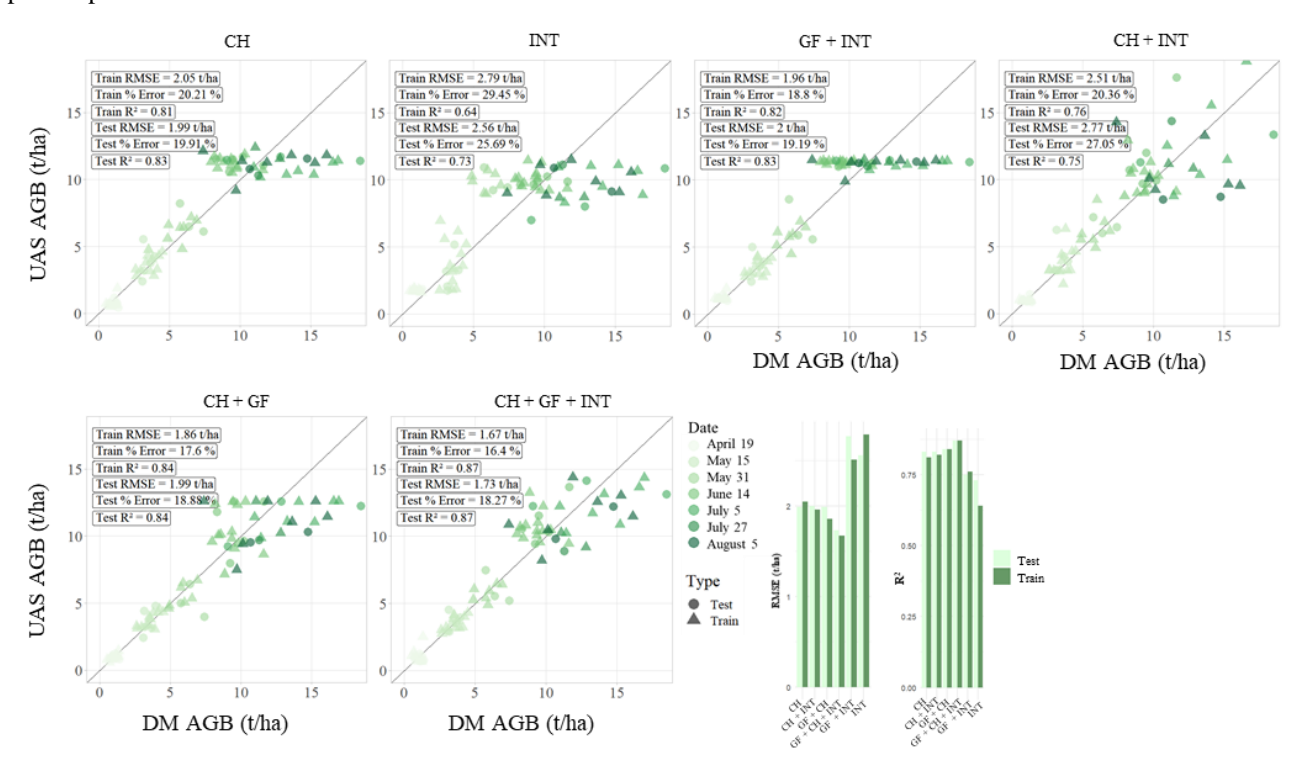


Figure 7: Biomass estimation performance using various combinations of LiDAR-derived metrics, including canopy height (CH), five-layer × 20 cm multi-layer gap fraction (GF), and signal intensity (INT). All models were trained using a GSD of 30 cm, corresponding to the best-performing GF configuration identified in earlier analysis.

CH alone provided strong predictive power (RMSE = 1.99 t/ha, R^2 = 0.83 testing), outperforming INT alone (RMSE = 2.56 t/ha, R^2 = 0.73). When combined, CH + INT did not improve upon CH alone, suggesting limited complementarity. However, integrating CH or INT with GF enhanced model performance. The combination of GF + CH achieved RMSE = 1.99 t/ha (R^2 = 0.84 testing), while adding INT further reduced RMSE to 1.73 t/ha (R^2 = 0.87 testing). This confirms that multi-dimensional structural information combined with LiDAR-derived signal intensity in the NIR contributes significantly to biomass estimation. The AGB maps produced with CH + GF + INT can be seen in the appendix with Figure A1.





5.3. Incorporation of LiDAR Metrics with MS Reflectance

The MS sensor data was subsequently evaluated both independently and in combination with the LiDAR-derived products, as illustrated in Figure 8.

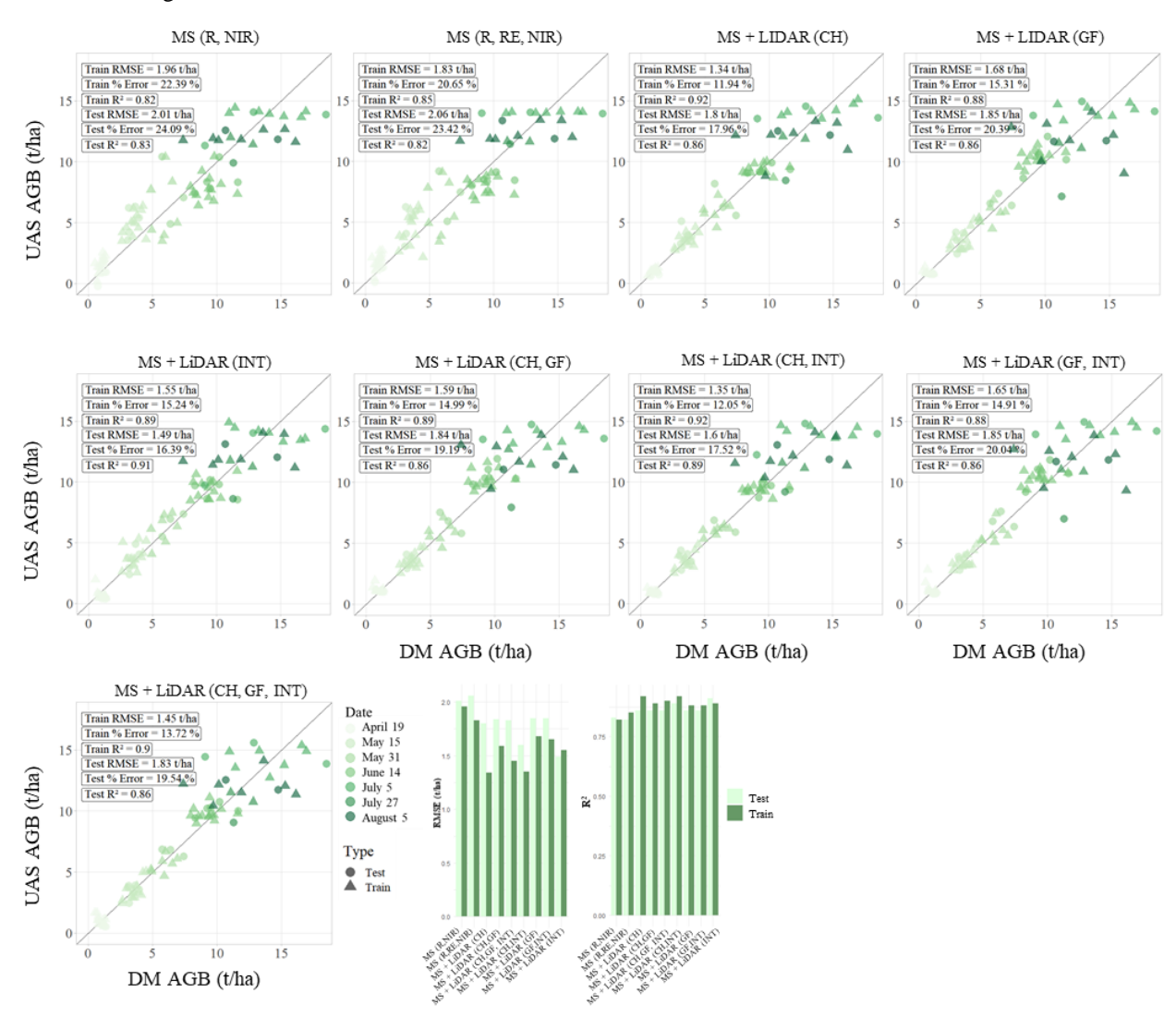


Figure 8: ANN model performance for biomass estimation using multispectral (MS) reflectance data alone and in fusion with LiDAR-derived features. Inputs include combinations of red (R), red-edge (RE), and near-infrared (NIR) bands with canopy height (CH), five-layer × 20 cm multi-layer gap fraction (GF), and signal intensity (INT). All models were trained using a GSD of 30 cm, corresponding to the best-performing GF configuration identified in earlier analysis.

We tested how MS data could enhance LiDAR-based models. Using MS bands alone (R, RE, NIR) yielded good results (RMSE = 2.06 t/ha, $R^2 = 0.82 \text{ testing}$), but performance improved when MS was combined with LiDAR-derived features. The most effective combinations involved MS + CH (RMSE = 1.80 t/ha, $R^2 = 0.86$) and MS + INT (RMSE = 1.49 t/ha, $R^2 = 0.91$).

MS + INT surpassed all single sensor uses. Combining all four LiDAR metrics (GF, CH, INT) with MS did not significantly



310

315



enhance performance further (RMSE = 1.83 t/ha, $R^2 = 0.86$), likely due to increased dimensionality and feature redundancy. Notably, MS + INT alone performed nearly as well as more complex combinations, indicating the complementary nature of these spectral features.

5.4. Incorporation of LiDAR Metrics and MS Reflectance with TIR Radiance

The TIR data were then added in evaluation alone and together with the LiDAR and MS products as can be seen in Figure 9.

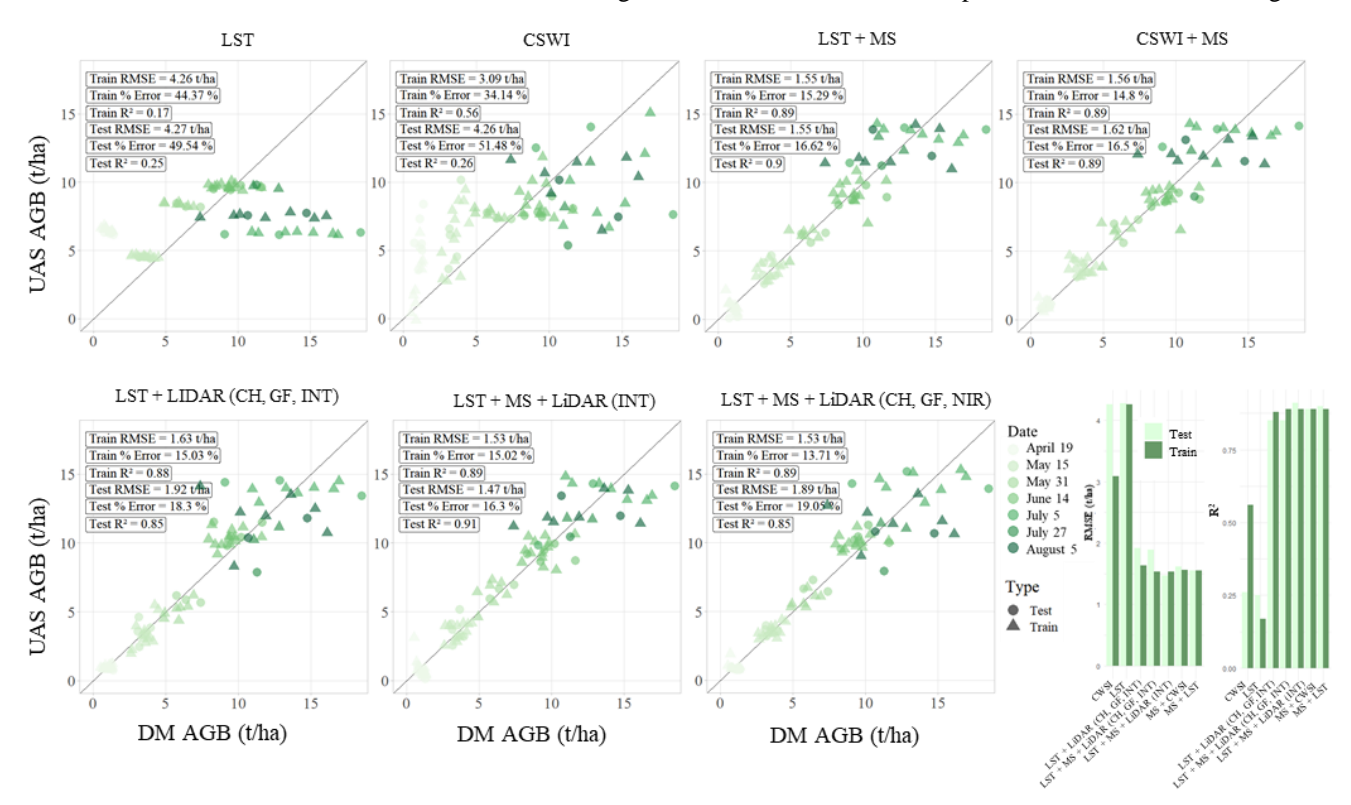


Figure 9: ANN model performance for estimating biomass using thermal infrared (TIR) data including land surface temperature (LST) and crop water stress index (CWSI) alone and in combination with multispectral (MS: red, red-edge, and near infrared) and LiDAR-derived features including canopy height (CH), five-layer \times 20 cm multi-layer gap fraction (GF), and signal intensity (INT). All models were trained using a 30 cm ground sampling distance (GSD), corresponding to the optimal GF configuration.

TIR radiance (LST) alone yielded poor biomass predictions (RMSE = 4.27 t/ha, $R^2 = 0.25$ testing). Incorporating the crop water stress index (CWSI) slightly improved performance (RMSE = 4.26 t/ha, $R^2 = 0.26$), but both remained far below LiDAR or MS metrics in accuracy. However, when TIR (LST) was combined with MS and LiDAR data, model performance improved significantly. The best-performing configuration overall was MS + INT + TIR (LST) (RMSE = 1.47 t/ha, $R^2 = 0.91$ testing). This fusion leveraged complementary structural and physiological signals, providing superior estimates across all growth stages. The addition of all LiDAR metrics to MS and TIR (i.e., MS + GF + CH + INT + TIR) did not outperform MS + INT +



335



TIR (LST), again suggesting diminishing returns from overly complex fusion. TIR thus plays a valuable supporting role when paired with spectral and structural information.

5.5. Overall Model Comparison and Ranking of Sensor Combinations

To clearly identify the best-performing individual and fused sensor configurations, we ranked the models based on their testing RMSE and R² across Sections 5.1 to 5.4 (Figure 10). These plots visually emphasize the superior performance of LiDAR-based models and the advantage gained through fusing complementary spectral and thermal features with LiDAR intensity. For single sensors, LiDAR-derived metrics combining CH, multi-layer GF, and INT consistently outperformed MS and TIR data. This underscores LiDAR's dual ability to capture structural and spectral canopy properties. MS performed better than TIR but fell short of LiDAR, especially during early and peak vegetative stages.

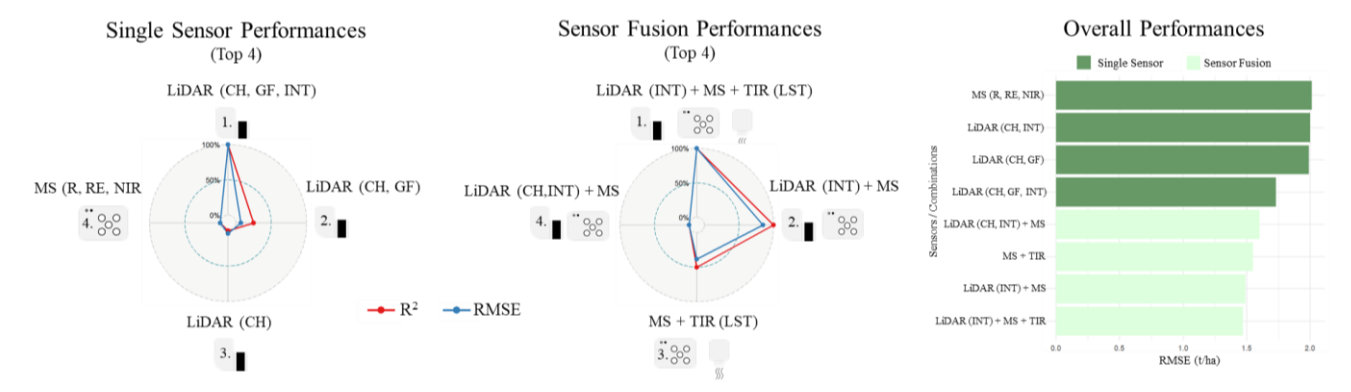


Figure 10. Radar plot comparing normalized RMSE and R² values for top-performing single sensors and sensor fusion combinations taken form section 5.1-5.4. Higher values indicate better model performance. LiDAR-derived features outperformed other single sensors, and the best-performing fusion combined LiDAR intensity (INT), MS, and TIR. Values are normalized within each group (single sensor vs. fusion).

Among fusion models, the combination of LiDAR INT, MS, and TIR achieved the best performance (RMSE = 1.47 t/ha, R² = 0.91). Notably, this configuration excluded CH and GF, suggesting that LiDAR INT effectively encapsulates both structural and physiological signals. This finding implies that intensity alone can serve as a compact yet information-rich LiDAR feature, reducing the need for complex multi-metric integration in some applications.

5.6. AGB Estimation Evaluation by Growth Phase

To further evaluate sensor performance over time, we analyzed the best-performing input combinations for each campaign date in addition to common configurations, considering both RMSE and R². Figure 10 summarizes the testing and training performance metrics across dates for single sensors and fusion models.



345

350



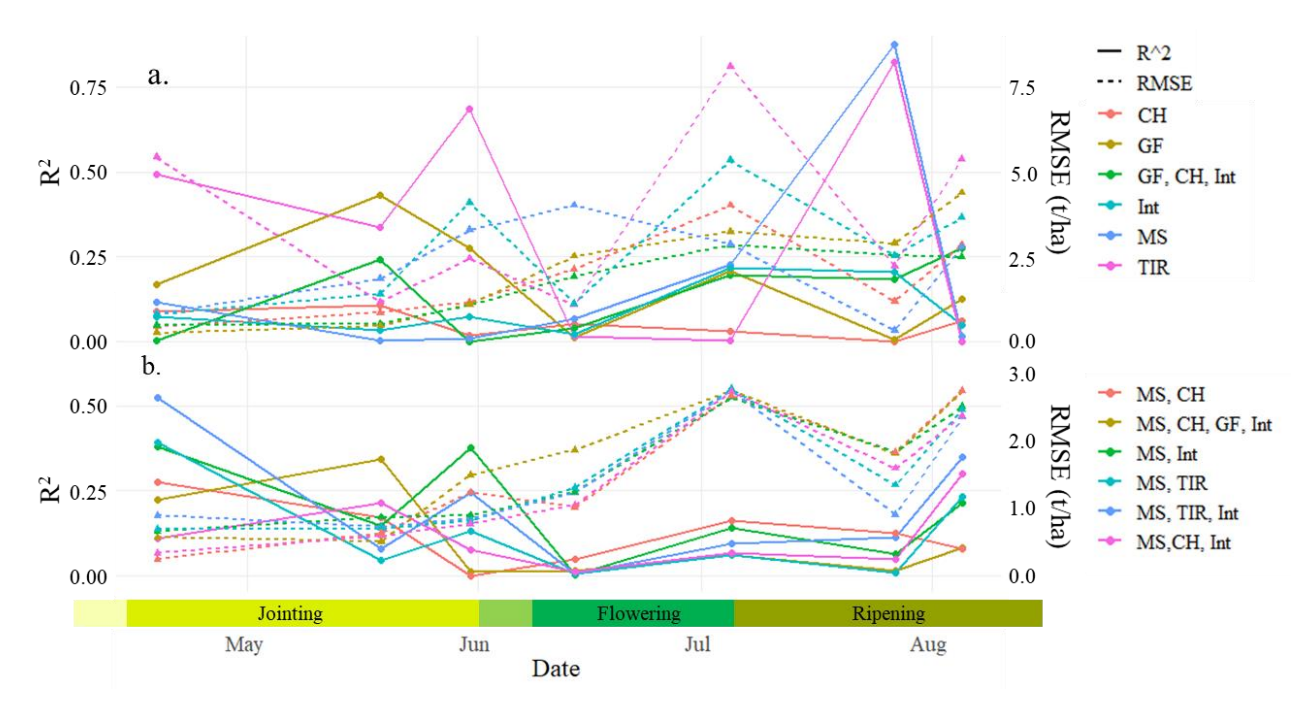


Figure 10: Performance (RMSE and R^2) of the ANN AGB estimation for each collection date within the different growing phases. The top graph (a) illustrates results for individual UAV sensor products, while the bottom graph (b) is fusion data from multiple sensors and their derived products. Sensor products include MS – Multispectral; CH – Crop height; GF – Gap Fraction; Int – LiDAR - intensity; TIR – Thermal infrared. The performances are based on the averages of the training and testing results.

Figure 11 provides a visual summary of the best-performing sensor configurations across campaign dates, illustrating how optimal inputs shifted throughout the growing season. In the early stages (e.g., April 19 and May 19), LiDAR-derived CH and multi-layer GF yielded the best performance, reflecting their sensitivity to initial structural development. As the canopy matured and closed (June through August), fusion models, particularly those combining MS and INT or MS + INT + TIR, consistently outperformed single-sensor approaches. These combinations proved especially effective under conditions of advanced growth and senescence. MS alone performed least effectively during the mid-season period, when spectral contrast was limited by uniformly high chlorophyll content, but improved again during ripening and senescence stages, where pigment degradation became a more pronounced indicator of crop status. This temporal shift in optimal sensor inputs emphasizes the importance of flexible, growth stage–specific integration strategies.



365

370



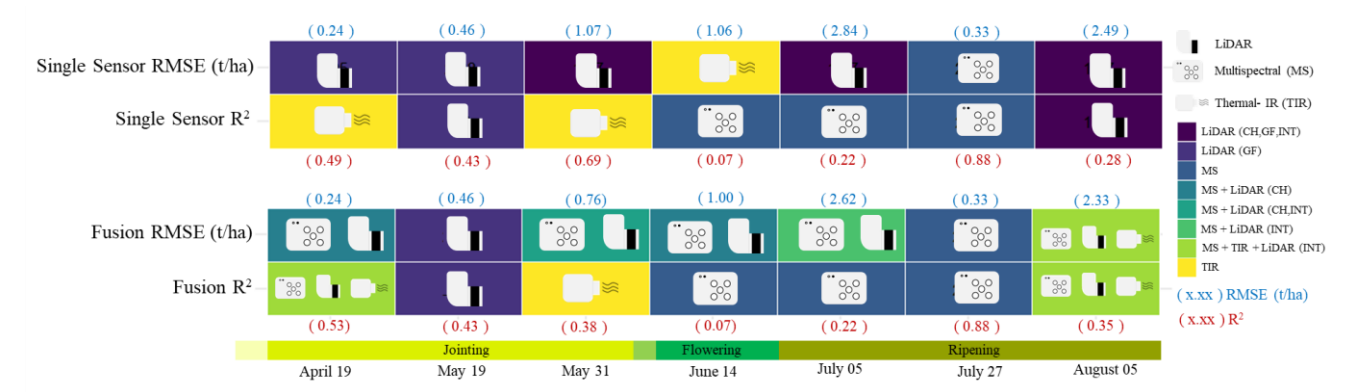


Figure 11: Best-performing single sensor and sensor fusion inputs for above-ground biomass (AGB) estimation across campaign dates, based on average RMSE and R^2 from training and testing data. Each tile shows the optimal input type for that date and metric (RMSE or R^2), with performance values overlaid.

5.7. Insights for Nitrogen Fertilization Monitoring

To assess the potential of UAV-derived AGB estimation for monitoring N treatment effects, average AGB values were compared across the three fertilization zones described in Section 2. These zones included 0%, 50%, and 100% of standard nitrogen application rates. Figure 12 presents a temporal comparison between UAV AGB estimates and ground-based destructive sampling (DM) across these zones. While the DM samples were limited to individual subplots, the UAV data reflect spatially continuous measurements across entire treatment sections.

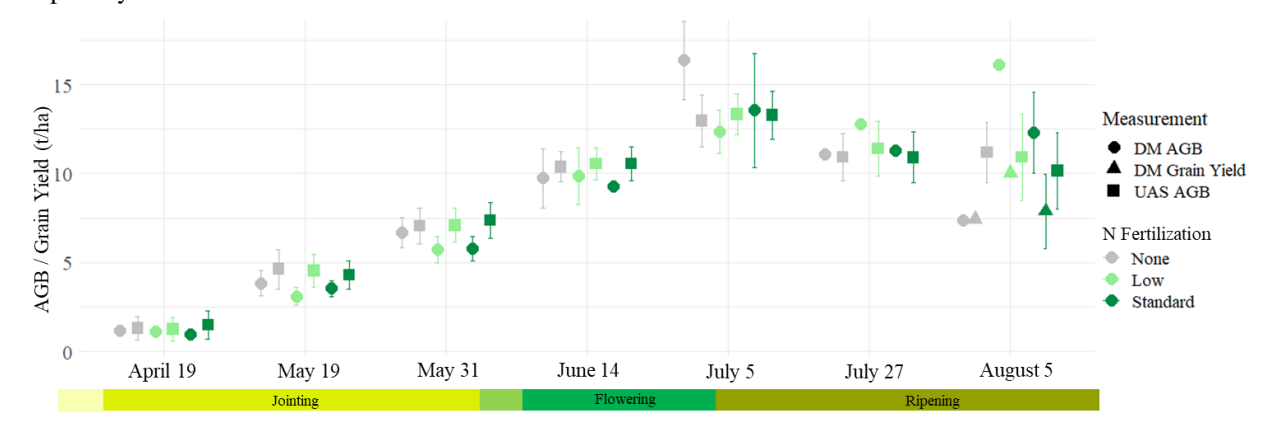


Figure 12: Comparison between UAV (entire plots inside treatment zone) and DM (specified measurement area of subplots) based AGB estimation for each nitrogen fertilization zone across key dates in the growing season.

Overall, UAV-derived estimates provided a more consistent and realistic depiction of spatial AGB variability than DM measurements, especially in later stages of the growing season (e.g., July 5 and August 5). Slight increases in AGB were detected in fertilized zones, particularly between the 0% and 50% N treatments. However, differences between the 50% and 100% N zones were less pronounced, possibly due to sampling limitations or environmental variability. These trends align with previous findings that show a positive correlation between N fertilization and biomass accumulation [15].





The UAV approach enabled detection of subtle spatial trends that would likely be missed using sparse destructive sampling alone. These results demonstrate the value of UAV platforms for supporting precision fertilization strategies. By delivering high-resolution, spatially explicit AGB estimates throughout the season, UAVs offer a scalable and timely alternative for nutrient monitoring.

6 Discussion

395

6.1. Enhancing AGB Estimation with Increased LiDAR Features and Optimized Parameters

Results demonstrated that LiDAR-derived structural features, particularly CH and GF, were strong individual predictors of AGB. Among different GF configurations, the use of five vertical GF layers (5 × 20 cm) and a 30 cm GSD yielded the highest accuracy. This multi-layer approach more accurately captured vertical canopy heterogeneity compared to conventional ground-only GF commonly used for LAI (Bates et al., 2021; Dreier et al., 2024) and AGB (Montzka et al., 2023; Hütt et al., 2022). Multi-layer GF proved particularly effective during peak canopy development, enabling spatial differentiation of structural density through signal returns concentrated in the upper canopy layers. Our approach directly incorporated these multi-layer GF inputs into the ANN, allowing the model to learn their relative importance throughout the season without additional parameterization as opposed to 3DPI. Notably, LiDAR INT, often overlooked or underutilized in UAV agriculture applications, contributed significantly improving the LiDAR's AGB estimation when used with CH and multi-layer GF. When all three of these LiDAR features are used, LiDAR alone outperformed the common combination of CH and MS. This could suggest, that INT helps alleviate the need for MS data for leaf pigment information.

6.2 Benefits of Multi-Sensor Fusion Across Phenological Stages

Fusion of LiDAR, MS, and TIR data yielded the most robust models, outperforming any individual sensor. This was particularly evident when combining MS spectral bands with LiDAR INT and TIR LST data. The complementary nature of these sensors became clear when evaluated temporally: early-season biomass predictions benefited most from CH and GF due to strong structural variation, while spectral (MS) and thermal (TIR) data became increasingly important during later stages when structural changes plateaued and physiological traits, such as chlorophyll degradation and peak evapotranspiration, dominated biomass variability.

Temporal performance shifts also highlighted the limitations of MS and TIR as stand-alone sensors. MS alone performed well during senescence but poorly during mid-season when vegetation was near spectral saturation. TIR, though limited in performance on its own, enhanced MS estimates when fused, primarily by contributing valuable information on canopy water status, including indicators of stomatal activity and evapotranspiration under high-temperature conditions. These results



405

410

415

420

425

430



underscore the advantages of multi-sensor integration for capturing the full complexity of crop development, particularly across distinct physiological growth stages.

6.3 LiDAR Intensity: A Compact, Informative Proxy

The most surprising finding was the strong performance of LiDAR INT when incorporated into fusion models, whether using only LiDAR features or combining features from MS and TIR sensors. When paired with MS and TIR, INT outperformed more complex configurations that additionally included CH and GF structural data. This supports the hypothesis that INT, particularly in the NIR spectrum, is sensitive to leaf angle distribution (Tian et al., 2021), canopy density (Hütt et al., 2022), and pigment degradation during senescence.

As illustrated in Figure 5, this is evident where INT amplitudes align with point density profiles: larger, denser leaves create more uniform, reflective surfaces, increasing return amplitudes. However, on July 27 and August 5, alignment between INT and density profiles decreased during senescence, likely due to reduced NIR reflectance from browning vegetation. Practically, these results suggest that LiDAR INT can serve as a compact, information-rich input, potentially reducing model complexity by minimizing the need for additional LiDAR-derived structural metrics or spectral features from other sensors.

6.4 Toward Scalable Monitoring in Precision Agriculture

The ANN models developed in this study produced accurate AGB predictions across the full growing season and under varying nitrogen treatment levels. Compared to traditional destructive sampling, UAV estimates offered higher spatial resolution and complete coverage, enabling detection of subtle variations in crop development. Notably, UAV-derived AGB maps were more responsive to nitrogen-induced differences, particularly during early and mid-season growth, highlighting their potential to support more precise nutrient management strategies. The UAV estimates also aligned more closely with applied treatment amounts, demonstrating that improved AGB estimation directly enhances the monitoring of nitrogen effects and enables timely, targeted interventions.

Our results further support the use of flexible, stage-specific sensor combinations. Structural LiDAR metrics are particularly valuable for early-season monitoring, while fusion with spectral and thermal data becomes critical during reproductive and senescence stages. Importantly, multi-layer GF and MS features can be directly integrated into machine learning models without intermediate conversions, simplifying workflows for complex multi-sensor feature fusions and operational implementation of UAV crop monitoring.

6.5 Possible Limitations and Improvements

While this study focused on comparing sensor inputs for ANN AGB estimation, future research should explore the influence of alternative ML models, such as those discussed in Han et al. (2019). As Sharma et al. (2022) and Bazrafkan et al. (2023)



440

450

455

460

465



highlight, sensor performance can vary by crop type and ML method, particularly in species with differing canopy architectures (e.g., grasses vs. broadleaf crops). Broader testing across crop types would improve generalizability. A core limitation of ML biomass estimation remains the reliance on destructive sampling for model training, which limits scalability. While LiDAR-derived structural metrics may be more transferable across sites with similar crop geometries, spectral metrics are more sensitive to local soil, moisture, and light conditions.

Feature refinement offers additional opportunities. Further tuning of GF parameterization (e.g., optimal layer segmentation based on canopy structure, point density, or sensor settings) could improve model accuracy. Similarly, LiDAR INT calibration could benefit from in-field reflectance targets or correction for angle and range effects, although our setup (low altitude, flat terrain) likely minimized these influences.

445 **6.6 Operational Considerations and Outlook**

While multi-sensor UAV campaigns offer clear performance advantages, they also introduce logistical trade-offs. Each additional sensor increases payload weight, power consumption, flight time, and post-processing complexity. Additionally, the high cost of individual sensors makes their combined use less economically efficient. This study highlights the advantages of both individual and combined UAS sensor applications for AGB estimation, allowing farmers to balance potential accuracy improvements against logistical and financial constraints. It is also important to note that, while some sensors may not excel at estimating AGB during certain periods, they could be more strongly correlated with other critical agricultural. These additional correlations might justify the combined use of sensors for purposes beyond AGB estimation. The strong performance of LiDAR INT, particularly in fusion with MS, suggests that a streamlined configuration using just LiDAR and MS could offer a practical and efficient alternative in many operational scenarios. For applications focused on water stress or canopy temperature, TIR remains a valuable complement due to its unique physiological insights.

Looking ahead, the modeling framework developed in this study can be extended to other crops and environments, particularly those where vertical canopy structure and stress responses play a key role in yield formation. The direct use of LiDAR-derived CH, multi-layer GF, and INT as inputs in ANN models simplifies the analytical pipeline, supporting broader adoption of UAV LiDAR monitoring for season-long crop assessment.

Finally, the unique NIR sensitivity of LiDAR INT warrants deeper exploration. Unlike passive sensors, LiDAR can penetrate deeper into canopy layers, capturing spectral information from regions typically obscured due to occlusion and reflectance constraints. This capability adds significant value to vegetation analysis by enabling structural-spectral hybrid sensing. The development of multi-frequency LiDAR systems, as highlighted by Takhtkeshha et al. (2024), could further enhance this potential by providing a broader spectral response similar to MS sensors, while maintaining canopy penetration. These





advancements may position active LiDAR sensing as a powerful hybrid tool, bridging the gap between traditional MS sensors and full 3D canopy characterization, and expanding its role in precision agriculture.

7 Conclusion

This study highlights the value of UAV multi-sensor fusion for aboveground biomass estimation in winter wheat by integrating LiDAR structure (crop height (CH) and multi-layer gap fraction (GF)), LiDAR intensity (INT), multispectral (MS) reflectance, and thermal infrared (TIR) data. A first comprehensive comparison and fusion of all three sensor types for AGB estimation, including rarely used LiDAR GF and INT metrics, in contrast to the common reliance on MS indices and crop height. Among single-sensor inputs, LiDAR features were most effective, with intensity emerging as a compact, information-rich predictor that may encode both structural and physiological traits. Sensor fusion further improved performance, with the best model (INT + MS + TIR) achieving a testing RMSE of 1.47 t/ha (16.3%) and R² of 0.91 across the growing season. Feature relevance shifted with crop stage, with structural metrics more useful early to middle in the season, and spectral/thermal features contributing more during senescence and stress. UAV estimates also provided spatially complete insights into nitrogen fertilization effects that were more consistent than those from limited destructive sampling.

We applied an ANN to evaluate sensor combinations, leveraging its ability to capture feature interactions while being parametrized for a small dataset. While ANN was suitable in this context, future work should test additional machine learning models, as algorithm choice may influence feature rankings and conclusions. Overall, the findings underscore the importance of fully exploiting LiDAR's dual structural and spectral information, particularly INT, within sensor fusion frameworks to support robust and scalable UAV biomass monitoring.

485

490





Appendix

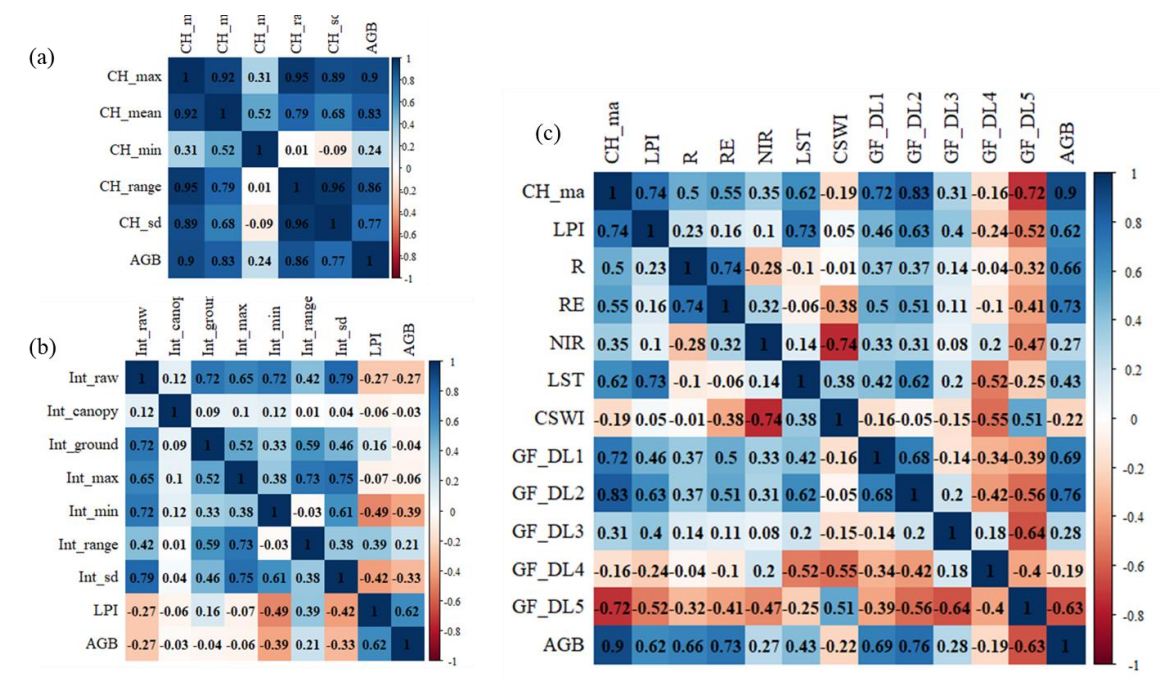


Figure A1. Correlation analysis of sensor-derived metrics with above-ground biomass (AGB). various LiDAR crop height (CH) metrics: maximum, minimum, standard deviation, range. mean. (b) LiDAR intensity (INT) metrics: raw unfiltered signal, canopy-only and ground-only returns, maximum and minimum intensity, range, standard deviation, and the Light Penetration Index (LPI), calculated by normalizing canopy intensity by the average ground intensity. (c) Combined correlation of maximum CH and LPI with spectral reflectance bands (Red, Red-edge, NIR), thermal products (LST, CWSI), and the 5×20 cm multi-layer LiDAR gap fraction (GF) density layers (DLs).

500





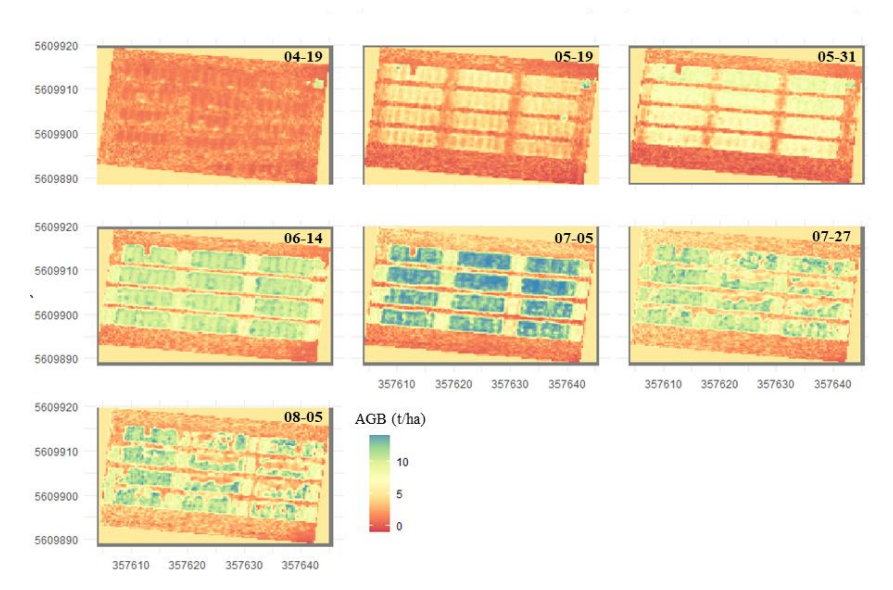


Figure A2. AGB estimation results per pixel for the field experiment site for each flight campaign date over the growing season using the combined use of LiDAR crop height (CH), multi-layer gap fraction (GF), and signal intensity (INT).

Data availability.

510

515

UAV LiDAR, multispectral, and thermal datasets used in this study are available from the corresponding author upon reasonable request.

Code availability.

All analyses were conducted in R using publicly available packages. The custom scripts for ANN training, LiDAR feature extraction, and sensor fusion workflows can be obtained from the corresponding author upon reasonable request.

520 Author Contributions

J.S.B., F.J., and C.M. conceived and designed the study. J.S.B. and R.B. collected the UAV and field data. J.S.B. performed the data analysis and wrote the manuscript. C.M., R.B., H.V., and F.J. contributed to manuscript review and editing. F.J., C.M., and H.V. supervised the research. All authors read and approved the final version of the manuscript.

525 Declaration of competing interest

There is no conflict of interest.





Acknowledgements

This research was supported by the Deutsche Forschungsgemeinschaft (DFG, German Research Foundation) under Germany's Excellence Strategy—EXC 2070—390732324, and by the Helmholtz Association through the Modular Observation Solutions for Earth Systems (MOSES) Initiative. The authors gratefully acknowledge Gina Lopez for providing the above-ground biomass measurements of the Milaneco winter wheat experiment.

References

535

- Bates, J. S., Montzka, C., Schmidt, M., & Jonard, F. (2021). Estimating Canopy Density Parameters Time-Series for Winter Wheat Using UAS Mounted LiDAR. Remote Sensing, 13(4), Article 4. https://doi.org/10.3390/rs13040710.
- Bates, J., Jonard, F., Bajracharya, R., Vereecken, H., & Montzka, C. (2022). Machine Learning with UAS LiDAR for Winter Wheat Biomass Estimations. AGILE: GIScience Series, 3, 1–4. https://doi.org/10.5194/agile-giss-3-23-2022.
- Bazrafkan, A., Delavarpour, N., Oduor, P. G., Bandillo, N., & Flores, P. (2023). An Overview of Using Unmanned Aerial System Mounted Sensors to Measure Plant Above-Ground Biomass. Remote Sensing, 15(14), Article 14. https://doi.org/10.3390/rs15143543.
- Bendig, J., Bolten, A., Bennertz, S., Broscheit, J., Eichfuss, S., & Bareth, G. (2014). Estimating Biomass of Barley Using Crop Surface Models (CSMs) Derived from UAV-Based RGB Imaging. Remote Sensing, 6(11), Article 11. https://doi.org/10.3390/rs61110395.
 - Berni, J. A. J., Zarco-Tejada, P. J., Suarez, L., & Fereres, E. (2009). Thermal and Narrowband Multispectral Remote Sensing for Vegetation Monitoring From an Unmanned Aerial Vehicle. IEEE Transactions on Geoscience and Remote Sensing, 47(3), 722–738. IEEE Transactions on Geoscience and Remote Sensing. https://doi.org/10.1109/TGRS.2008.2010457.
 - Biswal, S., Pathak, N., Chatterjee, C., & Mailapalli, D. R. (2024). Estimation of aboveground biomass from spectral and textural characteristics of paddy crop using UAV-multispectral images and machine learning techniques. Geocarto International, 39(1), 2364725. https://doi.org/10.1080/10106049.2024.2364725.
- Caturegli, L., Corniglia, M., Gaetani, M., Grossi, N., Magni, S., Migliazzi, M., Angelini, L., Mazzoncini, M., Silvestri, N., Fontanelli, M., Raffaelli, M., Peruzzi, A., & Volterrani, M. (2016). Unmanned Aerial Vehicle to Estimate Nitrogen Status of Turfgrasses. PLoS ONE, 11(6). https://doi.org/10.1371/journal.pone.0158268.



565

580



Cao, L., Liu, H., Fu, X., Zhang, Z., Shen, X., & Ruan, H. (2019). Comparison of UAV LiDAR and Digital Aerial Photogrammetry Point Clouds for Estimating Forest Structural Attributes in Subtropical Planted Forests. Forests, 10(2), Article 2. https://doi.org/10.3390/f10020145.

Dawidowicz, J., & Buczyński, R. (2025). Comparison of the Effectiveness of Artificial Neural Networks and Elastic Net Regression in Surface Runoff Modeling. Water, 17(3), 405. https://doi.org/10.3390/w17030405

Dreier, A., Lopez, G., Bajracharya, R., Kuhlmann, H., & Klingbeil, L. (2024). Structural wheat trait estimation using UAV-based laser scanning data: Analysis of critical aspects and recommendations based on a case study. Precision Agriculture, 26(1), 18. https://doi.org/10.1007/s11119-024-10202-4.

- Eitel, J. U. H., Magney, T. S., Vierling, L. A., Brown, T. T., & Huggins, D. R. (2014). LiDAR based biomass and crop nitrogen estimates for rapid, non-destructive assessment of wheat nitrogen status. Field Crops Research, 159, 21–32. https://doi.org/10.1016/j.fcr.2014.01.008.
- Gitelson, A. A., Viña, A., Arkebauer, T. J., Rundquist, D. C., Keydan, G., & Leavitt, B. (2003). Remote estimation of leaf area index and green leaf biomass in maize canopies. Geophysical Research Letters, 30(5). https://doi.org/10.1029/2002GL016450
 - Han, L., Yang, G., Dai, H., Xu, B., Yang, H., Feng, H., Li, Z., & Yang, X. (2019). Modeling maize above-ground biomass based on machine learning approaches using UAV remote-sensing data. Plant Methods, 15(1), 10. https://doi.org/10.1186/s13007-019-0394-z.
 - Heiskanen, J., Korhonen, L., Hietanen, J., & Pellikka, P. K. E. (2015). Use of airborne lidar for estimating canopy gap fraction and leaf area index of tropical montane forests. International Journal of Remote Sensing, 36(10), 2569–2583. https://doi.org/10.1080/01431161.2015.1041177.
- 585 Huang, W., Li, W., Xu, J., Ma, X., Li, C., & Liu, C. (2022). Hyperspectral Monitoring Driven by Machine Learning Methods for Grassland Above-Ground Biomass. Remote Sensing, 14(9), 2086. https://doi.org/10.3390/rs14092086
- Hütt, C., Bolten, A., Hüging, H., & Bareth, G. (2022). UAV LiDAR Metrics for Monitoring Crop Height, Biomass and Nitrogen Uptake: A Case Study on a Winter Wheat Field Trial. PFG Journal of Photogrammetry, Remote Sensing and Geoinformation Science, 91(2), 65–76. https://doi.org/10.1007/s41064-022-00228-6.



595



Jabed, Md. A., & Murad, M. A. A. (2024). Crop yield prediction in agriculture: A comprehensive review of machine learning and deep learning approaches, with insights for future research and sustainability. Heliyon, 10(24), e40836. https://doi.org/10.1016/j.heliyon.2024.e40836

Jimenez-Berni, J. A., Deery, D. M., Rozas-Larraondo, P., Condon, A. (Tony) G., Rebetzke, G. J., James, R. A., Bovill, W. D., Furbank, R. T., & Sirault, X. R. R. (2018). High Throughput Determination of Plant Height, Ground Cover, and Above-Ground Biomass in Wheat with LiDAR. Frontiers in Plant Science, 9. https://doi.org/10.3389/fpls.2018.00237.

- Johansen, K., Morton, M. J. L., Malbeteau, Y., Aragon, B., Al-Mashharawi, S., Ziliani, M. G., Angel, Y., Fiene, G., Negrão, S., Mousa, M. A. A., Tester, M. A., & McCabe, M. F. (2020). Predicting Biomass and Yield in a Tomato Phenotyping Experiment Using UAV Imagery and Random Forest. Frontiers in Artificial Intelligence, 3, 28. https://doi.org/10.3389/frai.2020.00028.
- Katimbo, A., Rudnick, D. R., Dejonge, K. C., Lo, T. H., Qiao, X., Franz, T.E., Nakabuye, H.N., & Duan, J. (2022). Crop water stress index computation approaches and their sensitivity to soil water dynamics. Agricultural Water Management, 266, 107575. https://doi.org/10.1016/j.agwat.2022.107575.
- Kidson, M., Nduku, L., Munghemezulu, C., Masiza, W., Nciizah, A., Adeleke, R., Rama, H., & Roopnarain, A. (2025).

 Applying Artificial Neural Networks and Multivariable Linear Regression from Unmanned Aerial Vehicle Datasets to Estimate Durum and Bread Wheat Yield under Low Nitrogen Application Rates (2025021307). Preprints. https://doi.org/10.20944/preprints202502.1307.v1
- Kim, S., McGaughey, R. J., Andersen, H.-E., & Schreuder, G. (2009). Tree species differentiation using intensity data derived from leaf-on and leaf-off airborne laser scanner data. Remote Sensing of Environment, 113(8), 1575–1586. https://doi.org/10.1016/j.rse.2009.03.017.
- Li, W., Niu, Z., Chen, H., Li, D., Wu, M., & Zhao, W. (2016). Remote estimation of canopy height and aboveground biomass of maize using high-resolution stereo images from a low-cost unmanned aerial vehicle system. Ecological Indicators, 67, 637–620 648. https://doi.org/10.1016/j.ecolind.2016.03.036.
 - Li, Y., Li, C., Cheng, Q., Duan, F., Zhai, W., Li, Z., Mao, B., Ding, F., Kuang, X., & Chen, Z. (2024). Estimating Maize Crop Height and Aboveground Biomass Using Multi-Source Unmanned Aerial Vehicle Remote Sensing and Optuna-Optimized Ensemble Learning Algorithms. Remote Sensing, 16(17), Article 17. https://doi.org/10.3390/rs16173176.



635



Liao, J., Zhou, J., & Yang, W. (2021). Comparing LiDAR and SfM digital surface models for three land cover types. Open Geosciences, 13(1), 497–504. https://doi.org/10.1515/geo-2020-0257.

Lionel, B. M., Musabe, R., Gatera, O., & Twizere, C. (2025). A comparative study of machine learning models in predicting crop yield. Discover Agriculture, 3(1), 151. https://doi.org/10.1007/s44279-025-00335-z

Liu, S., Baret, F., Abichou, M., Boudon, F., Thomas, S., Zhao, K., Fournier, C., Andrieu, B., Irfan, K., Hemmerlé, M., & Solan, B. de. (2017). Estimating wheat green area index from ground-based LiDAR measurement using a 3D canopy structure model. Agricultural and Forest Meteorology, 247, 12–20. https://doi.org/10.1016/j.agrformet.2017.07.007.

Lu, N., Zhou, J., Han, Z., Li, D., Cao, Q., Yao, X., Tian, Y., Zhu, Y., Cao, W., & Cheng, T. (2019). Improved estimation of aboveground biomass in wheat from RGB imagery and point cloud data acquired with a low-cost unmanned aerial vehicle system. Plant Methods, 15(1), 17. https://doi.org/10.1186/s13007-019-0402-3.

Ludovisi, R., Tauro, F., Salvati, R., Khoury, S., Mugnozza Scarascia, G., & Harfouche, A. (2017). UAV-Based Thermal Imaging for High-Throughput Field Phenotyping of Black Poplar Response to Drought. Frontiers in Plant Science, 8. https://doi.org/10.3389/fpls.2017.01681.

Luo, S., Chen, J. M., Wang, C., Gonsamo, A., Xi, X., Lin, Y., Qian, M., Peng, D., Nie, S., & Qin, H. (2018). Comparative
 Performances of Airborne LiDAR Height and Intensity Data for Leaf Area Index Estimation. IEEE Journal of Selected Topics in Applied Earth Observations and Remote Sensing, 11(1), 300–310. IEEE Journal of Selected Topics in Applied Earth Observations and Remote Sensing. https://doi.org/10.1109/JSTARS.2017.2765890.

Madec, S., Frederic, B., de Solan, B., Thomas, S., Dutartre, D., Jézéquel, S., Hemmerlé, M., Colombeau, G., & Comar, A.
 (2017). High-Throughput Phenotyping of Plant Height: Comparing Unmanned Aerial Vehicles and Ground LiDAR Estimates.
 Frontiers in Plant Science, 8. https://doi.org/10.3389/fpls.2017.02002.

Maimaitijiang, M., Ghulam, A., Sidike, P., Hartling, S., Maimaitiyiming, M., Peterson, K., Shavers, E., Fishman, J., Peterson, J., Kadam, S., Burken, J., & Fritschi, F. (2017). Unmanned Aerial System (UAS)-based phenotyping of soybean using multi-sensor data fusion and extreme learning machine. ISPRS Journal of Photogrammetry and Remote Sensing, 134, 43–58. https://doi.org/10.1016/j.isprsjprs.2017.10.011



675



Mesas-Carrascosa, F. J., Castillejo-González, I. L., de la Orden, M. S., & Porras, A. G.-F. (2012). Combining LiDAR intensity with aerial camera data to discriminate agricultural land uses. Computers and Electronics in Agriculture, 84, 36–46. https://doi.org/10.1016/j.compag.2012.02.020.

- Montzka, C., Donat, M., Raj, R., Welter, P., & Bates, J. S. (2023). Sensitivity of LiDAR Parameters to Aboveground Biomass in Winter Spelt. Drones, 7(2), Article 2. https://doi.org/10.3390/drones7020121.
- Morgan, G. R., Stevenson, L., Wang, C., & Avtar, R. (n.d.). UAS Remote Sensing for Coastal Wetland Vegetation Biomass Estimation: A Destructive vs. Non-Destructive Sampling Experiment. Remote Sensing, 17(14), 2335. https://doi.org/10.3390/rs17142335
- Neuville, R., Bates, J. S., & Jonard, F. (2021). Estimating Forest Structure from UAV-Mounted LiDAR Point Cloud Using Machine Learning. Remote Sensing, 13(3), Article 3. https://doi.org/10.3390/rs13030352.
 - Pan, L., Liu, L., Condon, A. G., Estavillo, G. M., Coe, R. A., Bull, G., Stone, E. A., Petersson, L., & Rolland, V. (2022). Biomass Prediction with 3D Point Clouds from LiDAR. 2022 IEEE/CVF Winter Conference on Applications of Computer Vision (WACV), 1716–1726. https://doi.org/10.1109/WACV51458.2022.00178.
- Richardson, J. J., Moskal, L. M., & Kim, S.-H. (2009). Modeling approaches to estimate effective leaf area index from aerial discrete-return LIDAR. Agricultural and Forest Meteorology, 149(6), 1152–1160. https://doi.org/10.1016/j.agrformet.2009.02.007.
- Roy Choudhury, M., Das, S., Christopher, J., Apan, A., Chapman, S., Menzies, N. W., & Dang, Y. P. (2021). Improving Biomass and Grain Yield Prediction of Wheat Genotypes on Sodic Soil Using Integrated High-Resolution Multispectral, Hyperspectral, 3D Point Cloud, and Machine Learning Techniques. Remote Sensing, 13(17), Article 17. https://doi.org/10.3390/rs13173482.
- Ruwanpathirana, P. P., Sakai, K., Jayasinghe, G. Y., Nakandakari, T., Yuge, K., Wijekoon, W. M. C. J., Priyankara, A. C. P., Samaraweera, M. D. S., & Madushanka, P. L. A. (2024). Evaluation of Sugarcane Crop Growth Monitoring Using Vegetation Indices Derived from RGB-Based UAV Images and Machine Learning Models. Agronomy, 14(9), Article 9. https://doi.org/10.3390/agronomy14092059.
- 690 Sabol, J., Patočka, Z., & Mikita, T. (2014). Usage of Lidar Data for Leaf Area Index Estimation. GeoScience Engineering, 60(3), 10–18. https://doi.org/10.2478/gse-2014-0013.



700

705

720



Saskai, T., Imanishi, J., Ioki, K., Song, Y., & Morimoto, Y. (2016). Estimation of leaf area index and gap fraction in two broad-leaved forests by using small-footprint airborne LiDAR. Landscape and Ecological Engineering, 12. https://www.springerprofessional.de/estimation-of-leaf-area-index-and-gap-fraction-in-two-broad-leav/11780700.

Scaioni, M., Höfle, B., Baungarten Kersting, A. P., Barazzetti, L., Previtali, M., & Wujanz, D. (2018). Methods from Information Extraction from LiDAR Intensity Data and Multispectral LiDAR Technology. The International Archives of the Photogrammetry, Remote Sensing and Spatial Information Sciences, XLII–3, 1503–1510. https://doi.org/10.5194/isprs-archives-XLII-3-1503-2018.

Seidel, S.J., Ahmadi, S.H., Weihermüller, L., Couëdel, A., Lopez, G., Behrend, D., Kamali, B., Gaiser T., & Hernández-Ochoa, I.M. (2024). The overlooked effects of environmental impacts on root:shoot ratio in experiments and soil-crop models. Science of The Total Environment, 955, 176738. https://doi.org/10.1016/j.scitotenv.2024.176738.

Sharma, P., Leigh, L., Chang, J., Maimaitijiang, M., & Caffé, M. (2022). Above-Ground Biomass Estimation in Oats Using UAV Remote Sensing and Machine Learning. Sensors, 22(2), Article 2. https://doi.org/10.3390/s22020601.

Smigaj, M., Agarwal, A., Bartholomeus, H., Decuyper, M., Elsherif, A., de Jonge, A., & Kooistra, L. (2024). Thermal Infrared Remote Sensing of Stress Responses in Forest Environments: A Review of Developments, Challenges, and Opportunities. Current Forestry Reports, 10(1), 56–76. https://doi.org/10.1007/s40725-023-00207-z.

Smith, D. T. L., Chen, Q., Massey-Reed, S. R., Potgieter, A. B., & Chapman, S. C. (2024). Prediction accuracy and repeatability of UAV based biomass estimation in wheat variety trials as affected by variable type, modelling strategy and sampling location. Plant Methods, 20(1), 129. https://doi.org/10.1186/s13007-024-01236-w

Solberg, S., Næsset, E., Hanssen, K. H., & Christiansen, E. (2006). Mapping defoliation during a severe insect attack on Scots pine using airborne laser scanning. Remote Sensing of Environment, 102(3), 364–376. https://doi.org/10.1016/j.rse.2006.03.001.

Takhtkeshha, N., Mandlburger, G., Remondino, F., & Hyyppä, J. (2024). Multispectral Light Detection and Ranging Technology and Applications: A Review. Sensors, 24(5), Article 5. https://doi.org/10.3390/s24051669.



740



- Tian, W., Tang, L., Chen, Y., Li, Z., Zhu, J., Jiang, C., Hu, P., He, W., Wu, H., Pan, M., Lu, J., & Hyyppä, J. (2021). Analysis and Radiometric Calibration for Backscatter Intensity of Hyperspectral LiDAR Caused by Incident Angle Effect. Sensors (Basel, Switzerland), 21(9), 2960. https://doi.org/10.3390/s21092960.
 - Tilly, N., Aasen, H., & Bareth, G. (2015). Fusion of Plant Height and Vegetation Indices for the Estimation of Barley Biomass. Remote Sensing, 7(9), Article 9. https://doi.org/10.3390/rs70911449.
 - Van Klompenburg, T. van, Kassahun, A., & Catal, C. (2020). Crop yield prediction using machine learning: A systematic literature review. Computers and Electronics in Agriculture, 177, 105709. https://doi.org/10.1016/j.compag.2020.105709
- Vahidi, M., Shafian, S., Thomas, S., & Maguire, R. (2023). Pasture Biomass Estimation Using Ultra-High-Resolution RGB UAVs Images and Deep Learning. Remote Sensing, 15(24), Article 24. https://doi.org/10.3390/rs15245714.
 - Wallace, L., Lucieer, A., Malenovský, Z., Turner, D., & Vopěnka, P. (2016). Assessment of Forest Structure Using Two UAV Techniques: A Comparison of Airborne Laser Scanning and Structure from Motion (SfM) Point Clouds. Forests, 7(3), Article 3. https://doi.org/10.3390/f7030062.
 - Wang, D., Xin, X., Shao, Q., Brolly, M., Zhu, Z., & Chen, J. (2017). Modeling Aboveground Biomass in Hulunber Grassland Ecosystem by Using Unmanned Aerial Vehicle Discrete Lidar. Sensors, 17(1), Article 1. https://doi.org/10.3390/s17010180.
- Wang, T., Liu, Y., Wang, M., Fan, Q., Tian, H., Qiao, X., & Li, Y. (2021). Applications of UAS in Crop Biomass Monitoring: A Review. Frontiers in Plant Science, 12, 616689. https://doi.org/10.3389/fpls.2021.616689
- Wu, Q., Zhong, R., Dong, P., Mo, Y., & Jin, Y. (2021). Airborne LiDAR Intensity Correction Based on a New Method for Incidence Angle Correction for Improving Land-Cover Classification. Remote Sensing, 13(3), Article 3.
 https://doi.org/10.3390/rs13030511.
 - Yang, Y., Qiu, J., Zhang, R., Huang, S., Chen, S., Wang, H., Luo, J., & Fan, Y. (2018). Intercomparison of Three Two-Source Energy Balance Models for Partitioning Evaporation and Transpiration in Semiarid Climates. Remote Sensing, 10(7), Article 7. https://doi.org/10.3390/rs10071149.
 - You, H., Wang, T., Skidmore, A. K., & Xing, Y. (2017). Quantifying the Effects of Normalisation of Airborne LiDAR Intensity on Coniferous Forest Leaf Area Index Estimations. Remote Sensing, 9(2), Article 2. https://doi.org/10.3390/rs9020163.





Zhang, W., Qi, J., Wan, P., Wang, H., Xie, D., Wang, X., & Yan, G. (2016). An Easy-to-Use Airborne LiDAR Data Filtering
Method Based on Cloth Simulation. Remote Sensing, 8(6), Article 6. https://doi.org/10.3390/rs8060501.